



Cite this: *Biomater. Sci.*, 2023, **11**, 6504

Fabrication and *in vitro* investigation of hyperbranched poly-lysine-grafted warp knitted polypropylene sling for potential treatment of stress urinary incontinence†

Shuying Zhao,^{a,b} Meiqi Fang,^{a,b} Yan Li, ^{*a,b} Fujun Wang,^{a,b} Hao Li^c and Lu Wang ^{a,b}

Polypropylene (PP) sling implantation is the most commonly performed procedure for women with stress urinary incontinence (SUI). However, concerns have arisen regarding complications caused by slings, including the common issue of erosion, which can be attributed to various factors such as the body's response and bacterial contamination. To address these concerns, we have developed a rectangular mesh self-locking edge sling with a large pore size and lightweight design. Promising results have been obtained from preliminary *in vivo* mechanical reliability tests, including uniaxial tensile tests. In comparative *in vitro* fixed load tensile tests and simulated Tension-free Vaginal Tape (TVT) and Transobrotator Vaginal Tape inside-out (TVT-O) technique tests using commercial slings, our sling demonstrated less transverse wrinkling. Both slings achieved an effective porosity of over 45% under the TVT technique. However, the commercial sling experienced a significant reduction in effective porosity during the TVT-O technique, whereas our sling maintained a stable effective porosity with minimal wrinkling. Furthermore, we successfully developed cationic hydration rejection-driven antibacterial-anti-fouling coatings on the surface of our sling by grafting hyperbranched poly-lysine (HBPL) mediated by polynorepinephrine. The HBPL coating imparts a positive charge and hydrophilicity to the sling, resulting in elevated bactericidal activity and reducing protein adhesion. An optimal grafting concentration of 20 mg mL⁻¹ was selected, confirming the stability and biocompatibility of the sling coating. This coating is expected to reduce the likelihood of postoperative erosion. Overall, our research represents significant advancements in improving the safety and performance of PP slings for stress urinary incontinence, potentially leading to a reduction in complications following surgery.

Received 1st June 2023,
Accepted 7th August 2023
DOI: 10.1039/d3bm00943b
rsc.li/biomaterials-science

1. Introduction

Stress urinary incontinence (SUI) is a common urinary system disorder in middle-aged and elderly women.¹ According to statistics, approximately 20–40% of women worldwide suffer from SUI, with the prevalence reaching 50–70% among women aged 50 and above.² In the United States, around 25–50% of women are affected, with annual treatment costs exceeding 12 billion US dollars. It is estimated that the number of women

undergoing surgical treatment will increase from 210 700 in 2010 to 310 050 in 2050.³ In recent decades, the mid-urethral sling procedure has become the standard treatment for women with moderate to severe SUI or those with concomitant pelvic floor functional disorders.⁴

The surgical implantation of synthetic slings has greatly improved the cure rate for SUI patients. However, the medical device reported from the United States, pointed out that long-term follow-up investigations have revealed postoperative complications such as vaginal erosion, urethral erosion, urethral infection, and bladder perforation.^{5–7} In 2011, the U.S. Food and Drug Administration officially emphasized the risks of various complications, including vaginal erosion, associated with the use of mesh implants in the treatment of pelvic organ prolapse, while further evaluation is needed for the complications associated with synthetic mesh implantation in SUI surgeries.⁸ With increasing global attention to the compli-

^aKey Laboratory of Textile Science & Technology, Ministry of Education, College of Textiles, Donghua University, Shanghai, China. E-mail: yanli@dhu.edu.cn

^bKey Laboratory of Textile Industry for Biomedical Textile Materials and Technology, Donghua University, Shanghai, China

^cShanghai Hongyu Medical Technology Co., Ltd, Shanghai, China

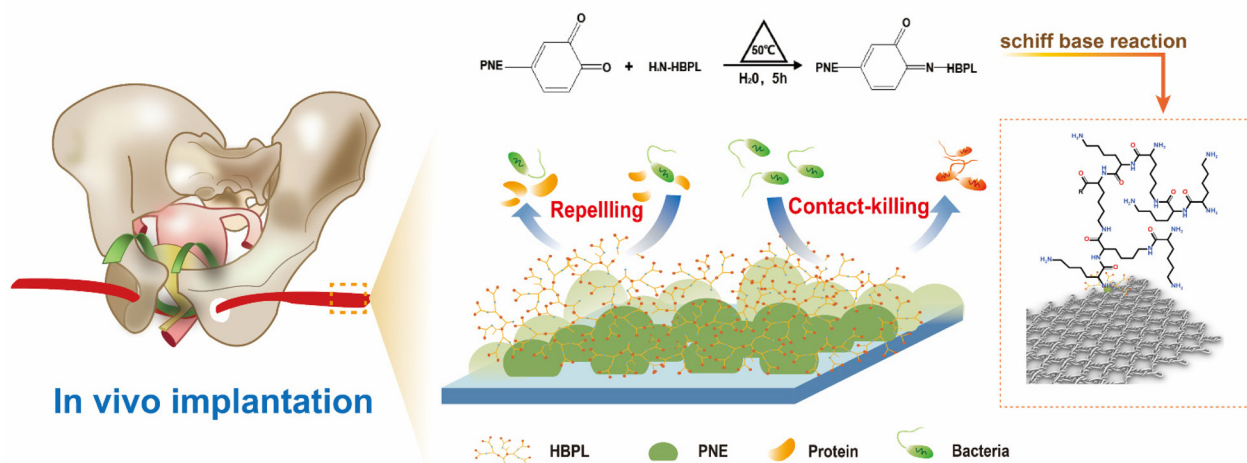
† Electronic supplementary information (ESI) available. See DOI: <https://doi.org/10.1039/d3bm00943b>

cations of mesh implant surgeries, reducing postoperative complications in SUI has become one of the current hot topics.

With the continuous improvement in medical standards and the quality of physicians, the physical properties of slings and bacterial infections have become the main factors influencing erosion.^{9–11} The most commonly used slings for clinical implantation are lightweight and large-pored polypropylene monofilament meshes, with a diamond mesh structure being predominant.¹² The most typical example is the TVT series sling manufactured by Johnson & Johnson.¹³ As the pore size increases and the mesh density decreases, the sling tightens under intra-abdominal pressure. Its elongated structure makes it prone to curling and wrinkling.¹⁴ Excessive deformation can lead to a decrease in effective porosity.¹⁵ When the porosity becomes less than 1 mm, the mesh can be filled with fibroblasts and collagen tissue, resulting in poorly healed hard scar tissue. The overall increase in mesh stiffness will cause stress shielding in the sling, leading to thinning and degeneration of deep tissues. Consequently, sling products exhibit more severe erosion issues after surgery compared to other mesh repair materials.^{16–18} Knight *et al.* implanted contracted and collapsed slings and flat slings separately in the vaginal canal of rhesus monkeys. After 12 weeks, animals implanted with deformed meshes showed significant complications.¹⁹ The mesh led to vaginal epithelial exposure, fibroblast proliferation, and fibrosis, resulting in pain. This confirmed that sling contraction and a decrease in effective porosity were key factors in postoperative erosion. In addition to these factors, the method of edge formation also affects the erosion of the material on nearby soft tissues.²⁰ Zdenek Rusavy *et al.* compared the efficacy of mechanically cut and laser-cut tension-free vaginal closure slings and found that mechanically cut slings with lower hardness experienced relaxation within 2 weeks after implantation, while laser-cut slings with higher

hardness exhibited better stability.²¹ However, the edge formation of the cut type resulted in a “sawtooth” appearance of the sling edge, and the rough edge inevitably caused damage to surrounding tissues. Further research is needed to explore trauma-preventing methods for sling edge formation.

Bacterial infection is another important factor that triggers sling erosion problems. Sling erosion caused by bacterial infection occurs in two main ways. Firstly, surface bacterial infections on the sling can lead to evident postoperative complications, such as acute urinary tract infections, cellulitis, necrotizing fasciitis, and osteomyelitis.¹⁰ Secondly, bacterial colonization on the sling’s surface can impede proper cell adhesion and fibrotic reactions, potentially resulting in incompatibility between the sling and the host, leading to erosion or compression and severely impacting normal vaginal wound healing.⁸ As a derivative of hernia repair meshes, the research on the antimicrobial functionalization of slings can draw lessons from patch-related studies.²² This is mainly achieved by incorporating antimicrobial agents, such as antibiotics, metal ions or nanoparticles, antimicrobial peptides, and cationic polymers, into the surface of the patch to form an antimicrobial coating.^{23–26} For example, Labay *et al.* plasma-functionalized PP slings and then coated the surface with nano-scale polyethylene glycol as a drug delivery system, loading ampicillin as an antibacterial drug.²⁷ The drug loading increased from 20.8% to 59.5%, demonstrating excellent antibacterial activity and biocompatibility. However, compared to the abdominal wall, the complex microenvironment of the vagina imposes higher requirements on the antimicrobial performance of sling surfaces.²⁸ The vagina is considered a “clean-contaminated” surgical area, with *Staphylococcus aureus* (*S. aureus*), *Staphylococcus epidermidis*, and *Escherichia coli* (*E. coli*) being part of the patient’s endogenous microbial flora, which may reside in the vagina before or during surgery. Sling implanted through the vagina inevitably experiences bacterial



Scheme 1 Scheme of the preparation of the sling. It has a smaller degree of wrinkling and better retention of effective porosity, and can reduce bacterial infection through antibacterial and anti-adhesive effects and effectively avoid postoperative erosion.

adhesion during the surgical process, and bacterial colonization on the mesh can affect the accessibility of host cells to the material surface, thereby interfering with normal cell adhesion and tissue integration.^{29,30} This exacerbates foreign body reactions, leading to premature erosion caused by sling-tissue separation and displacement. At the same time, antimicrobial functionalized surfaces cannot prevent protein adsorption and adhesion. Proteins adsorbed on the scaffold can serve as a nutrient matrix for bacterial adhesion and proliferation, ultimately leading to the failure of antimicrobial functionality.³¹ Therefore, surfaces with single antimicrobial functionality are often difficult to meet the requirements of vaginal implantation.

In this work, intending to reduce postoperative erosion rate, we have designed a sling with a stable woven structure, low contraction rate, and no edge-cutting effect, based on being lightweight, large-pored, and having a high effective porosity. The sling was then surface-modified to achieve dual functionality of antibacterial and anti-adhesive properties (Scheme 1). First, using polypropylene monofilaments as knitting material, we fabricated a rectangular mesh self-locking edge sling and compared it with a commercially available diamond mesh sling with laser-cut edges. By examining the basic structural parameters and conducting *in vitro* mechanical property tests on the sling, as well as analyzing the deformation mechanism of different tissues under stress induction, we demonstrated the structural advantages of the sling in reducing postoperative erosion. Subsequently, taking into account the differences in surface characteristics of the materials, inspired by the mussel-inspired biomimetic materials, we oxidized and self-polymerized norepinephrine (NE) to form poly-norepinephrine (PNE) on the surface of the sling, and facilitated the interaction between HBPL and the surface of the substrate to construct a strong, durable dual-functional surface with antibacterial and anti-adhesive properties. This achieved a synergistic reduction of sling postoperative erosion.

2. Materials and methods

2.1 Materials

Commercial Slings (PI 38) were purchased from Medprin Regenerative Medical Technologies Co., Ltd. Medical grade polypropylene monofilaments were supplied by Shanghai Hongyu Medical Tech Co, Ltd (China). NE was purchased from Aladdin Co., Ltd (China). L-Lysine hydrochloride was obtained from Aladdin Co., Ltd (China). Tris(hydroxymethyl)amino-methane, potassium hydroxide, sodium hydroxide, and sodium dodecyl sulfate (SDS) were purchased from Sinopharm Chemical Reagent Co., Ltd (China). ϵ -Polylysine (ϵ -PL) was obtained from Zhengzhou Binafo Bioengineering Co., Ltd (China). The BCA protein concentration assay kit and total antioxidant capacity assay kit were supplied by Shanghai Biyuntian Biotechnology Co., Ltd (China). The *S. aureus* strain

and *E. coli* strain were provided by Shanghai Bioresource Collection Center (China).

Human skin fibroblasts (HFF) were supplied by the Chinese Academy of Sciences' Cell Bank (Shanghai, China). Fetal bovine serum (FBS), penicillin–streptomycin solution (PS), Trypsin (EDTA), sodium pyruvate, and L-glutamine were purchased from Gibco (USA). Cell Counting Kit-8 (CCK-8) was provided by Shanghai Yisheng Biotechnology Co., Ltd.

2.2 Slings knitting stitch design

All slings were fabricated on a raschel machine, RS4EL (Runyuan Medical Supplies Technology Co., Ltd, Changzhou, Jiangsu, China), gauge E12 with an electronic guide bar control system. The knitting schemas and chain notation of newly designed meshes are presented in Table 1.

The images of the slings were captured by a stereoscopic microscope (Shanghai Cewei Photoelectric Technology Co., Ltd, China). The pixel values of the images are counted to find the porosity and effective porosity.

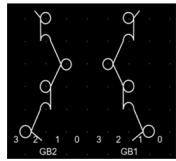
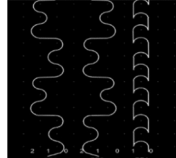
2.3 Mechanical properties of slings

2.3.1 Constant load tensile property test. Uniaxial tensile testing used a YG(B)026G electronic fabric strength tester (Wenzhou Darong Textile Instrument Co., Ltd, China). The clamping length was 20 mm, and the stretching speed was 100 mm min⁻¹.^{32,33} After that, the specimens were loaded to 2.5 and 16 N cm⁻¹ with the same clamping length and stretching speed, held for 60 s, and then returned to the initial state and relaxed for 180 s. The tension was repeated 3 times and the force and deformation of the sling were recorded.

2.3.2 Three-point beam bending test. Concerning the normal position of the sling material in the physiological structure of the pelvis and the predicted force, the sling is subjected to a three-point bending test with a fixed load using a textile stiffness tester (Suzhou Shengte Intelligent Technology Co., Ltd, China) to realize an *in vitro* test of the *in vivo* force simulation of the sling.

Briefly, the motor is controlled to move the needle down to the initial position of the urethra, *i.e.* 40 mm below the specimen table, and the specimen table spacing is set to 40 mm and 80 mm, respectively. Subsequently, the sling was cut into specimens with a size of 40 cm \times the forming width, passed through the press pin in a tension-free state, and placed on the horizontal surface of the specimen table. The ends were fixed using long-tail clips instead of collets to simulate the intraoperative fixation of the sutures at both ends. During the test, 200 cN was used as the bending force and 60 mm min⁻¹ as the vertical movement speed of the compression needle. The force-displacement curve of the specimen was also extracted, and visual images of the contact area between the sling and the compression needle before and after compression were taken to calculate the transverse crumpling rate. The porosity and effective porosity were tested in the same way as before.

Table 1 The knitting schemas and chain notation of two types of slings

Sample	Chain notation	Density (g mm ⁻²)	Large pore size (mm)	Porosity (%)	Effective porosity (%)	Knitting schemas
PI 38	GB1: 1-0/1-2/2-1/2-3/2-1/1-2// GB2: 2-3/2-1/1-2/1-0/1-2/2-1//	4.64 × 10 ⁻⁵	1.55 ± 0.08	67.82 ± 0.70	55.62 ± 0.12	
PP	GB1: 0-2/2-0//4// GB2: 4-4/2-2/4-4/0-0/2-2/0-0// GB3: 0-0/2-2/0-0/4-4/2-2/4-	4.0 × 10 ⁻⁵	1.88 ± 0.06	73.55 ± 2.50	57.17 ± 1.00	

2.4 Preparation and characterization of functionalized slings

2.4.1 Preparation of HBPL. L-Lys (27.3 g) was dissolved in 30 mL of ultrapure water and neutralized with 1 : 1 KOH (8.4 g) in a three-necked round-bottom flask. The flask was connected to a nitrogen stream and stirred with a sealed overhead electronic stirrer at 150 °C for 48 h. At the end of the reaction, the product was fully dissolved with 30 mL of dilute HCl at 0.06 N, transferred to a dialysis bag, and immersed in 1 L of deionized water for two days, with water changes every 12 h. The polymer HBPL was freeze-dried and stored at -20 °C.

A Fourier transform infrared (FTIR) spectroscopy (PerkinElmer, USA) with an attenuated total reflectance (ATR) attachment was used to scan the powdered samples of the reaction monomer L-Lys and the polymerization product HBPL over the scan range of 500–4000 cm⁻¹.

The composition, molecular structure, and branching of HBPL were tested using NMR spectroscopy. The degree of branching (DB) is an important indicator of the degree of branching of HBPs, defined as the ratio of the molar fraction of branched chains and terminal units associated with the total number of possible branching sites. The DB values were calculated according to eqn (1) proposed by Hawker *et al.*³⁴

$$DB = \frac{D + T}{D + L + T} \quad (1)$$

The number of branches (ANB) was calculated according to eqn (2) proposed by Hölter *et al.*³⁵

$$ANB = \frac{D}{D + L} \quad (2)$$

where *D*, *T* and *L* are the molar fractions of the dendritic, terminal and linear units of the HBPLs, respectively, which were obtained by integrating the corresponding peaks of the ¹H-NMR spectra to obtain the molar fractions of the structural units using the Mestrelab Research (Spain) Mestre nova software.

The commercial poly(lysine) ε-PL and the synthetic HBPL were prepared into 1 mg mL⁻¹ solution using 5 mM NaCl solution, and the particle size, PDI, and surface zeta potential of

the polymers were measured using a zeta-potential analysis and particle size analyzer (Malvern Panalytical, UK).

2.4.2 Preparation of HBPL- and PNE-functionalized slings. A Tris-HCl buffer solution (0.1 M pH 8.5) was used as the solvent to prepare 2 mg mL⁻¹ of NE solution, and clean PP slings were completely submerged in NE solution and oxidized and self-polymerized for 24 h in a constant temperature shaker (37 °C, 60 rpm) and in an aerobic environment. At the end of the process, the surface of the specimens was washed well with deionized water and dried. The untreated sling samples were labeled as PP, and the treated sling samples were labeled as PNE-PP.

HBPL solution (ultra-pure water as solvent) was prepared at 5 mg mL⁻¹, 10 mg mL⁻¹, 20 mg mL⁻¹, and 30 mg mL⁻¹. And PNE-PP was impregnated in it and shaken in a shaker at 50 °C for 5 h for grafting with different concentrations of HBPL solution. After the reaction, the treatment was shade dried at room temperature. The resulting modified sling samples were labeled as 5HBPL-PNE-PP, 10HBPL-PNE-PP, 20HBPL-PNE-PP, and 30HBPL-PNE-PP, respectively.

2.4.3 Characterization of HBPL- and PNE-functionalized sling. To analyze the type and distribution of chemical groups on the surface of the samples, the sling samples were tested and analyzed by Fourier transform infrared spectroscopy. Surface chemistry and elemental analysis were characterized using X-ray photoelectron spectroscopy (XPS, Thermo Fisher Scientific, USA). The water contact angle was measured to compare the wettability of all samples by a static water contact angle measurement system (DataPhysic, Germany).

The area of the sling discs with *d* = 3.5 mm was calculated and weighed, and the increment of the modified gram weight of the sling with respect to the blank control PP was used as the grafting amount of the coating. A 25 mL solution of 0.01 M HCL was prepared in a centrifuge tube, and the samples were placed in a shaker at 25 °C for 2 h. After the reaction, the grafting amount was calculated as the grafting amount.

After the reaction, 120 μL of 0.1% phenolphthalein indicator was added dropwise to the solution, and the titration was neutralized with 0.01 M NaOH solution, and the titration was completed when the phenolphthalein changed from colorless

to light pink and did not fade after 5 min. The amino content in samples was calculated as follows:

$$A = \frac{C_{\text{NaOH}}(V_0 - V)}{g} \quad (3)$$

where A is the amino content ($\mu\text{mol mg}^{-1}$), C_{NaOH} is the sodium hydroxide concentration (mol L^{-1}), V_0 is the volume of sodium hydroxide solution consumed in the blank control sample (mL), V is the consumption volume of sodium hydroxide solution (mL), and g is the weight of the sample (mg).

For the quantitative characterization of the material surface charge properties, a solid surface zeta potential tester was used for the determination by the flow potential method. The samples (1×2 cm) before and after modification were tested in 1 mM KCl solution at pH 6.5. The surface morphology of the samples was observed by scanning electron microscopy (Hitachi, Japan) at an acceleration voltage of 15 kV.

2.5 Antibacterial performance

2.5.1 Antibacterial rates. Gram-negative bacteria *E. coli* (ATCC 25922) and Gram-positive bacteria *S. aureus* (ATCC 29213) were cultured in LB medium at 37 °C overnight and adjusted to (1×10^8 CFU mL^{-1}) in 0.1 M PBS (pH = 7.4). Before testing, the stent samples were cut into small round pieces ($d = 1.4$ cm) and sterilized with 75% ethanol. Each test group comprised three specimens. All tests were carried out at 37 °C.

Samples were immersed in test tubes containing 100 μL of diluted bacterial suspension (10^5 CFU mL^{-1} of the bacterium) and shaken at 120 rpm for 15 h. After incubation, the suspension was harvested and the bacteria enumerated.

2.5.2 Bacterial morphology. The morphology of the bacteria on the surface of two different samples was observed by FE-SEM. In brief, 300 μL of bacterial suspension (10^6 CFU mL^{-1}) was co-cultured with each sample in a 24-well plate at 37 °C for 4 h. At the end of the reaction, the samples were sonicated and the obtained bacterial suspension was centrifuged at 8000 rpm for 5 min to collect the cell precipitate, after which 4% paraformaldehyde was added to fix it for 4 h. The bacteria were then dehydrated by gradient ethanol (30%, 50%, 70%, 80%, 90%, and 100% v/v) in sequence, each for 15 min. Finally, the bacteria were dried in a vacuum oven and sputtered with gold for FE-SEM observation.

2.6 Anti-adhesion properties

2.6.1 Antibacterial adhesion activity. For the bacterial adhesion test, the samples were placed in test tubes and covered with 1 mL of diluted bacterial suspension containing 10^8 CFU mL^{-1} of each bacterium under aseptic conditions. The samples were incubated for 4 h with continuous shaking at 120 rpm. After 4 h each sample was rinsed several times with PBS solution to remove any nonadherent bacteria and sonicated in PBS solution for 15 min to detach the adherent bacteria. An aliquot of the suspension (100 μL) was harvested and serially diluted ($\times 10^1$, $\times 10^2$, and $\times 10^3$) for plating on the LB agar for bacterial enumeration.

2.6.2 Antiprotein adsorption activity. The slings were cut into small discs of $d = 1.4$ cm, fixed in 2 mg mL^{-1} of BSA/PBS solution, and adsorbed in a shaker at 37 °C and 60 rpm for 6 h.

After the reaction, multiple washes with PBS were used. A 2% SDS solution was prepared and 100 μL of each well was added to the washed specimens, and the adsorbed proteins were eluted in a constant temperature shaker at 37 °C and 60 rpm. After elution, the eluate and BCA working solution were added to the wells at a ratio of 1 : 10 and incubated for 0.5 h. The OD values were then measured.

2.7 The coating stability of HBPL-PNE-PP

2.7.1 Static stability. The *in vitro* degradation was conducted in the sterilized PBS under 37 °C and samples were harvested at 1, 3, 5, and 7 d. The SEM images of the samples at each period were observed respectively.

2.7.2 Dynamic stability. Wet samples (soaked in PBS for 2 h) were stretched to the constant load of 16 N cm^{-1} circularly using a YG(B)026G-500 tensile strength tester (Wenzhou Darong Textile Instrument Co., Ltd, China). The coating morphology of the most severely stressed part was observed by SEM. After that, the antibacterial test of the sample was carried out according to the experimental steps of 2.6.

2.7.3 Anti-oxidation property. The sling samples were cut into 1×1 cm squares, placed in a 24-well plate, and 1 mL of sterilized PBS buffer solution (pH 7.4) was added dropwise to three of the parallel samples. (pH 7.4), and the reaction was carried out at 37 °C for 24 h in a constant temperature shaker at 60 rpm. When finished, wash and dry. Add FRAP working solution (180 μL) was added dropwise to each well to completely infiltrate the specimen, and incubated in a 37 °C water bath for 5 min. The OD value was also read. The standard curve equation was used to calculate the antioxidant value of each specimen and the average value was taken.

2.7.4 Friction stability. In order to observe the frictional stability of the coating, transparent adhesive tape was used for the adhesion treatment, and the coating morphology was observed. The shape of the coating was observed under a scanning electron microscope before and after the test. Three pieces of 2×2 cm tapes were cut and gently attached to the adhesive side of the tape using tweezers. The tape was gently attached to the adhesive side of the tape with tweezers, folded, and glued for 10 s. The tape was then gently torn along the edge of the tape. After 10 s, the tape was gently peeled off along the edge, and then the tape was lifted with forceps. The samples were observed by SEM and compared with the untaped group. The samples were compared with the unadhered group.

2.8 Cell viability and proliferation

After leaving human skin fibroblast cells (HFF, density = 4×10^4 cells per well) to complete attachment in a 24-well plate, test samples were placed in the medium; a group without samples was set as the blank control (BC). After co-incubation for 1, 3, and 7 d, cells were re-cultured in Dulbecco's modified

Eagle's medium (DMEM, Life Technologies, USA) containing cell counting kit-8 reagent (CCK-8, 10% v/v, Yusheng Biotechnology, China) for 2 h. The optical density (OD) values at 450 nm were read using a microplate spectrophotometer ($n = 3$ for each group).

3. Results and discussion

3.1 Design and performance characterization of slings

Regarding the design of slings, the traditional commercial sling PI 38 adopts a diamond-shaped structure, as shown in Fig. 1a. This organizational structure is woven by two sets of combs in a variable warp satin weave pattern, with one set passing through while the other set remains empty. The two sets of combs form a closed diamond-shaped mesh with a staggered arrangement through symmetrical weft padding. Additionally, edge shaping is achieved through laser cutting to minimize fraying.

For our designed PP sling, we chose a large aperture rectangular mesh, as shown in Fig. 1b. This organizational structure is formed by combining the warp chain organization with

the lining weft through three sets of combs. The open chain serves as the ground organization to reduce the longitudinal extensibility of the mesh. The other two sets of combs weave the lining weft, forming interlaced long lining weft in the basic unit mesh loops, providing both transverse connection and longitudinal reinforcement. This increases the stability of the square mesh structure, making it more effective in reducing the longitudinal stretching of the sling under load and minimizing transverse wrinkling. Furthermore, leveraging the organizational advantages of the PP sling, we obtained a self-locking edge strip by drawing yarn from the finished fabric.

Currently, the development trend in clinical applications of slings is lightweight, large mesh openings, and high effective porosity of warp-knitted mesh.¹⁴ While meeting the mechanical performance requirements for implantation, a higher effective porosity in the mesh is more conducive to the favorable integration of the sling with the vagina. The measurement of sling porosity is shown in Fig. S1,† indicating that both types of slings are large-aperture meshes with an effective porosity exceeding 55% under static conditions. The PI 38 sling has a maximum aperture length of 1.55 mm, with a porosity of 67.82%, and an effective porosity of 55.62%. On the other hand, the PP sling has a maximum aperture length of 1.88 mm, with a porosity of 73.55% and an effective porosity of 57.17%. Both the aperture size and effective porosity of the PP sling slightly outperform the commercially available PI 38 sling.

Under a width of 1 cm, the highest load the sling experiences in the body when the bladder is full does not exceed the force exerted by the intravesical pressure, which is 16 N. The ideal tensile strength of a sling should be greater than or equal to 2 N.^{32,36}

The stress–strain curves of the slings are shown in Fig. S2.† The rupture strengths of PI 38 and PP are 38.95 N cm^{-1} and 38.49 N cm^{-1} , respectively, which are significantly higher than the required strength, meeting the stress–strain requirements for implantation. The elastic modulus of PP is 20.24 MPa, noticeably higher than the 7.09 MPa of the PI 38 sling, indicating that our designed PP sling exhibits better dimensional stability.

Due to the unique ribbon-like slender structure of the slings, after implantation in the human body, they may curl, fold, and wrinkle, thereby reducing the effective porosity. When the pore size is too small, the woven threads are prone to be filled with fibroblasts and collagen tissue, forming scar plates and inducing adverse integration through bridging encapsulation. This results in more severe erosion issues for sling products compared to other mesh repair materials.^{18,19} Therefore, examining the pore and deformation conditions of the sling under a certain tensile load can effectively reflect its mechanical performance. Generally, intravesical pressure is used to evaluate the pressure exerted on materials in the urethral area.

The deformation of both slings under different tensile forces is shown in Fig. 2a. From Fig. S2b and 2c,† it can be observed that when not under tension, the porosity and

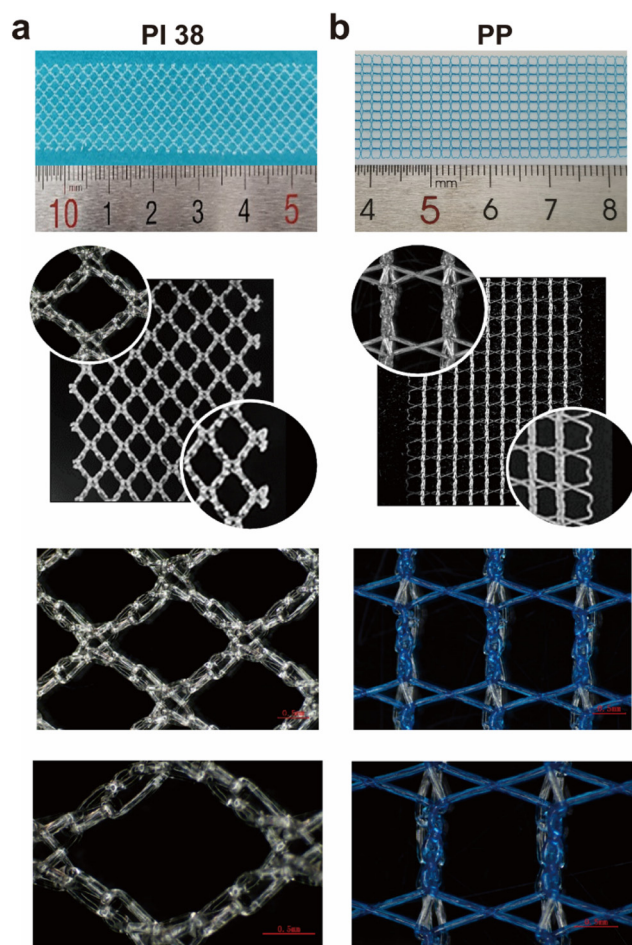


Fig. 1 Mesh characteristics and edge molding types for PI38 (a) and PP (b).

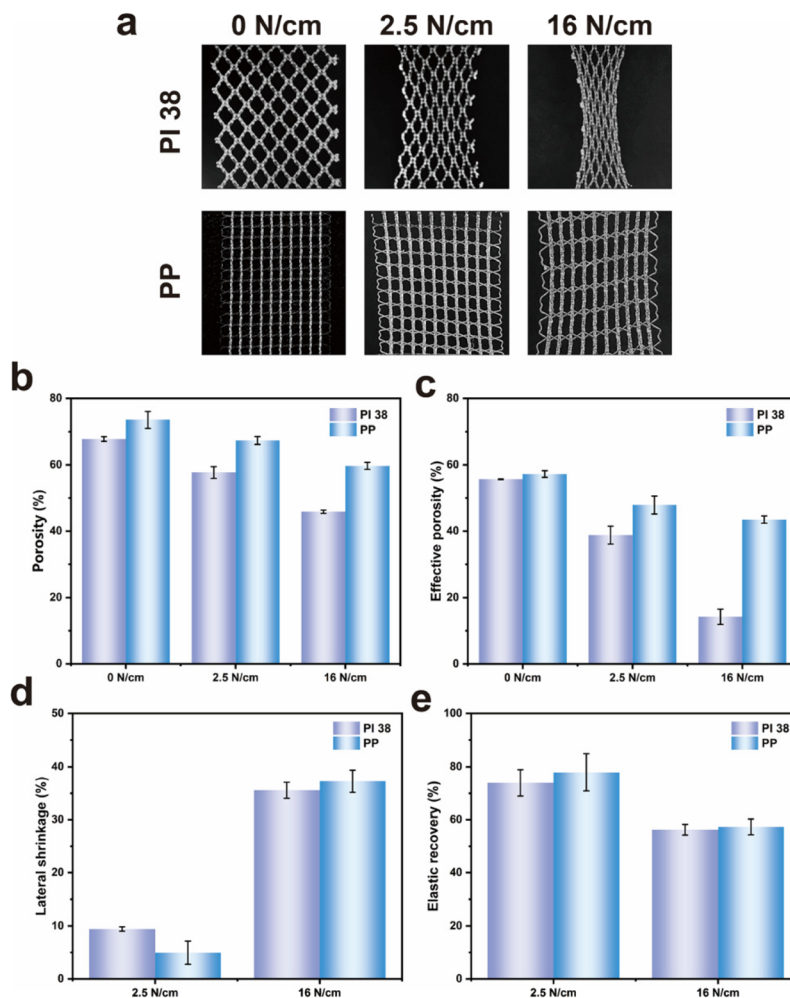


Fig. 2 Sling elongation performance at constant load. (a) Photos after stretching. (b) Porosity of two types of slings before and after stretching. (c) Effective porosity of the two types of slings before and after stretching. (d) Lateral shrinkage rate of two types of slings after stretching. (e) Elastic recovery rate of two types of slings after stretching.

effective porosity of PI 38 are 67.82% and 55.62%, respectively, while for PP, they are 73.55% and 57.17%, respectively. Under a force of 2.5 N, the porosity of PI 38 and PP decreases to 57.67% and 67.38%, respectively, with effective porosities of 38.8% and 47.87%. Under a force of 16 N, the porosity of PI 38 and PP is 45.85% and 59.68%, respectively, with effective porosities of 14.23% and 43.46%. It is evident that compared to PI 38, PP maintains a higher effective porosity under different tensile forces. The transverse wrinkling rates of PI 38 and PP under a force of 2.5 N are 9.44% and 4.97%, respectively, while under a force of 16 N, they are 35.56% and 37.28%, indicating that the organizational structure of the PP sling with warp-knitted rectangular mesh has an advantage in reducing wrinkling (Fig. 2d).

Furthermore, the wrinkling of the sling is not only related to fabric dimensional stability but also to elasticity. Due to variations in surgeons' experience, excessive stretching of elastic slings can lead to pore failure and even transverse urethral incisions. The elastic recovery rates of the PP sling under

2.5 N and 16 N forces are 77.87% and 57.30%, respectively, both higher than those of the commercially available PI 38 sling (73.94% and 56.25%) (Fig. 2e). PP exhibits better elasticity, which is advantageous in reducing the decrease in sling pore size caused by surgical traction.

After implantation, the sling exists in a "hammock" form. The flexural rigidity can represent the flexibility of the mesh. If the flexural rigidity is too low, it may affect the suspension of the sling due to excessive softness or cause curling and create a "cutting effect" on the tissue under compression. On the other hand, if the flexural rigidity is too high, it may affect the mechanical compatibility with adjacent tissues and lead to erosion. As an implantable material, two-dimensional analysis of forces cannot accurately represent the three-dimensional forces experienced by the sling inside the body, and it does not align well with the bending forces acting on the sling within the body. Therefore, by borrowing the three-point bending test function of a textile stiffness tester and considering different surgical procedures and initial positions, an

in vitro three-dimensional force testing model was established to simulate the sling's internal forces in the human body.^{37,38}

In the classic TVT procedure, a tension-free sling is positioned at approximately 20 mm from the midline on both sides of the urethra, utilizing small incisions of about 5 mm each. On the other hand, the TVT-O procedure involves the sling passing 40 mm laterally from the midline on each side, forming a 90° angle after fixation. Considering the diameter of the urethra, in TVT, the distance between the lower end of the sling and the abdomen is approximately 40 mm, and the distance between the two fixed points of the sling is also 40 mm. While in TVT-O, these distance increases to 80 mm.

In the context of pelvic organ support, the tension-free sling is anchored at both ends to fixed points on each side, while the middle portion experiences forces and bending due to contact with the surrounding organ. Brandão *et al.*³⁹ conducted finite element simulations to compare the corrective capabilities of lower stiffness Mesh_{LS} and higher stiffness

Mesh_{HS} slings on the urethra. Assuming a scenario with combined damage to the anal sphincter and pubourethral ligament, both types of slings reduced the displacement of the bladder, urethra, and bladder neck from rest to maximum Valsalva maneuver. The forces exerted by Mesh_{HS} were higher (2.3 N and 3.4 N, respectively) than those exerted by Mesh_{LS}. However, due to the higher forces applied by Mesh_{HS} on the urethral wall, there is a possibility of increased risks of vaginal erosion and urinary retention. Consequently, it is speculated that the tension forces acting on the full-length tension-free vaginal sling in the female pelvic structure are approximately 2 N or greater. Therefore, a maximum applied force of 2 N is used to load the sling in the body, and the subsequent observations include the sling's wrinkling and changes in effective porosity.

The testing methods for both procedures are shown in Fig. 3a. From the displacement-flexural force curve of the sling in Fig. 3b, it can be observed that under the TVT-O procedure,

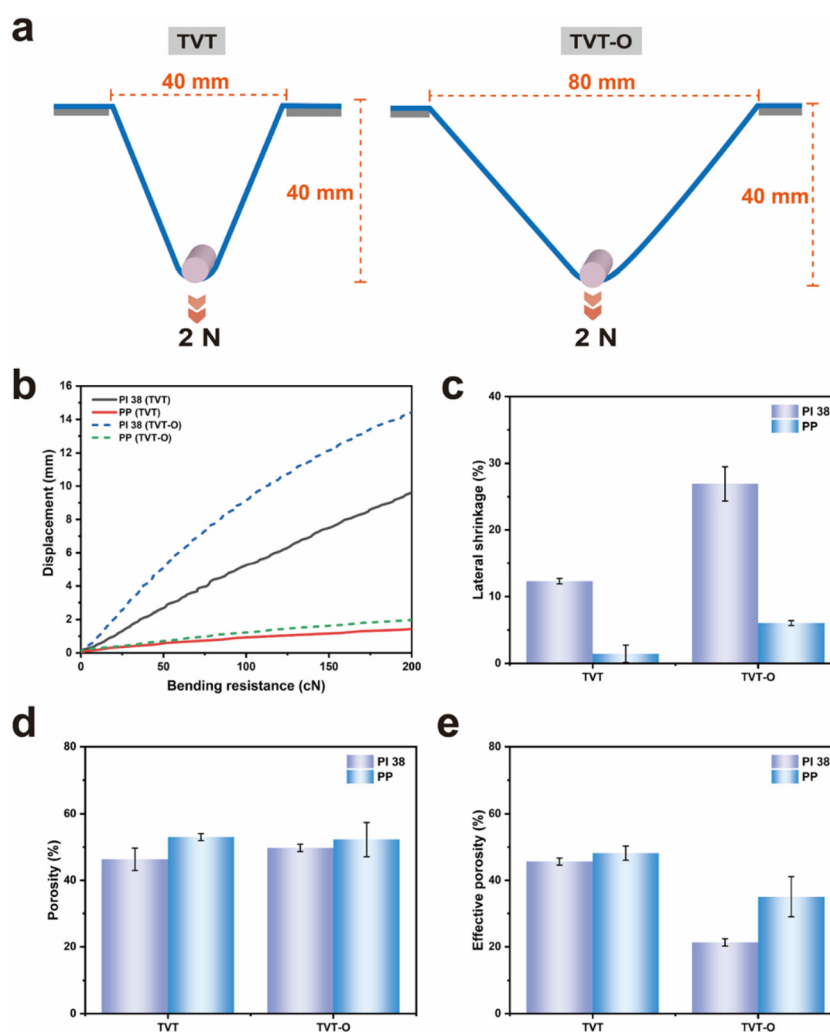


Fig. 3 Sling bending force simulation *in vitro* (a) sling force simulation under TVT, TVT-O technique. (b) Displacement–bending force curve. (c) Lateral shrinkage rate of the slings in the bending test (d) porosity rate of two types of slings after stretching. (e) Effective porosity rate of the slings in the bending test.

both PI 38 and PP exhibit smaller displacement and bending deformation compared to the TVT procedure. This is because the TVT-O procedure has a larger relative angle of implantation, and after the vertical force of the urethra is distributed along the sling, the forces reaching the sides of the sling gradually decrease. Furthermore, whether under the TVT or TVT-O procedure, the displacement of PI 38 is greater than that of PP, indicating that PI 38 has lower flexural rigidity and is more flexible.

Under both procedures, the transverse wrinkling rates of PP are only 1.44% and 6.04%, respectively (Fig. 3c), further confirming that in the pelvic force environment inside the body, when the bladder is full, the transverse wrinkling of the sling is smaller for PP, effectively avoiding wrinkling. Conversely, the wrinkling rate of PI 38 reaches 12.30% and 26.93%, respectively. This is because the diamond mesh structure of PI 38 is more prone to elongation, and the inclined warp-knitted loops in the structure are more likely to stretch inward and upward. Additionally, the porosity and effective porosity of PI 38 are correspondingly smaller (Fig. 3d and e). Under the TVT procedure, both slings achieve an effective porosity of over 45%, with PP slightly higher than PI 38. Under the TVT-O procedure, PP still maintains an effective porosity of 35.05%. Thus, in terms of maintaining a good effective porosity, PP has a greater advantage compared to PI 38 in the simulated in-body force conditions.

In conclusion, the mechanical properties of the commercial PI 38 and PP slings both meet the requirements for in-body implantation. The rectangular mesh structure of PP and its edge self-locking design make it superior in terms of wrinkle resistance and resistance to pore failure, thus reducing sling erosion issues.

3.2 Construction of antibacterial-anti-adhesive functionalized sling

Based on the previous testing, PP slings have greater structural advantages in reducing the probability of postoperative erosion compared to commercially available PI 38 slings. Furthermore, to address the issue of sling erosion caused by bacterial infection, an interface-repellent-driven antibacterial-anti-adhesive coating was successfully constructed on the surface of inert PP material using mussel-inspired adhesive PNE assist hyperbranched HBPL modification.

The synthesis process of HBPL is shown in Fig. 4a. HBPL was prepared through “thermally initiated” polymerization. During the polymerization process, the clear transparent solution gradually turned yellow. As a result of the thermally initiated dehydration condensation forming peptide bonds, the solution gradually became viscous. After a continuous reaction for 48 hours, a brownish-yellow viscous liquid was obtained, which was then dialyzed and freeze-dried to obtain the bright yellow solid shown in Fig. 4a.

Fig. 4b shows the FTIR spectra of the monomers Lys and HBPL. The peak at 3280 cm^{-1} in the HBPL spectrum indicates the presence of N-H, which comes from the primary and tertiary amines in the molecular structure. The peak at 2930 cm^{-1}

is related to the asymmetric and symmetric stretching vibrations of methylene in HBPL. The strong peaks at 1637 cm^{-1} and 1535 cm^{-1} (amide I and II bands) are caused by the stretching vibrations of amide, proving the formation of peptide bonds. Compared to the Lys spectrum, HBPL contains all the characteristic peaks of Lys, and the absorption peaks in the amide I and II bands are blue-shifted, indicating the conversion of primary amines to secondary amines.

To further confirm the successful polymerization of Lys into HBPL, $^1\text{H-NMR}$ was used to determine the molecular structure of the polymerization product, calculate the degree of branching and average branching number. From the $^1\text{H-NMR}$ spectrum in Fig. 4c, the chemical shifts at $\delta = 4.17$ correspond to the dendritic unit (D) in the HBPL molecular structure, 3.89 corresponds to the α -linear unit (α -L), 3.37 corresponds to the terminal unit (L), and 3.28 corresponds to the ϵ -linear unit (ϵ -L).³⁵ Generally, the OB value of linear polymers is 0, the OB value of dendritic polymers is 1, and the OB value of HBPs is usually between 0.4 and 0.6. A higher OB value indicates better branching, and the molecular structure is closer to a perfect three-dimensional dendritic polymer.³⁴ The integrated moles of the corresponding units were obtained as 5.38, 1.00, 3.06, and 10.23, respectively, resulting in an OB value of 0.429 and an ANB of 0.324, which falls within a reasonable range, indicating that the synthesized polymerization product has a well-formed hyperbranched structure.

Fig. 4d shows the comparison of particle size and polydispersity index (PDI) between commercial ϵ -PL and HBPL. By comparing the results, it can be seen that the molecular size of HBPL is 66.61 nm with a PDI of 0.466, which is much smaller than the size of ϵ -PL (2566 nm) and its PDI (1.000). This indicates that the synthesized HBPL particles have a smaller size and a more uniform molecular distribution in the solution system. Furthermore, as shown in Fig. 4e, the surface potential of HBPL molecules is 19.07 mV, exhibiting a positive charge that is approximately three times higher than that of ϵ -PL (3.55 mV). Therefore, it can be inferred that if PNE-PP slings are treated with an equivalent reaction concentration, HBPL polymer with a smaller size and higher zeta potential would have an advantage in achieving higher grafting density and improving the material's surface positive charge within a unit area.

NE is a neurotransmitter derivative, similar to dopamine, that can undergo oxidative self-polymerization on the majority of material surfaces under weak alkaline conditions, leading to the formation of a nanoscale PNE coating. This PNE coating creates a biomimetic interface with robust hydrophilicity, chemical stability, and abundant functional reaction sites, resulting in a highly adhesive biomimetic interface.

Leveraging the strong adhesiveness of PNE, we adopted a simple and environmentally friendly one-step method to activate and modify the inert PP sling, forming a dense and super-smooth biomimetic film on the sling's surface. Subsequently, by utilizing the Schiff base reaction between the terminal amino groups of the HBP linker and the surface oxidized quinone groups, we guided HBPL grafting onto the sling's

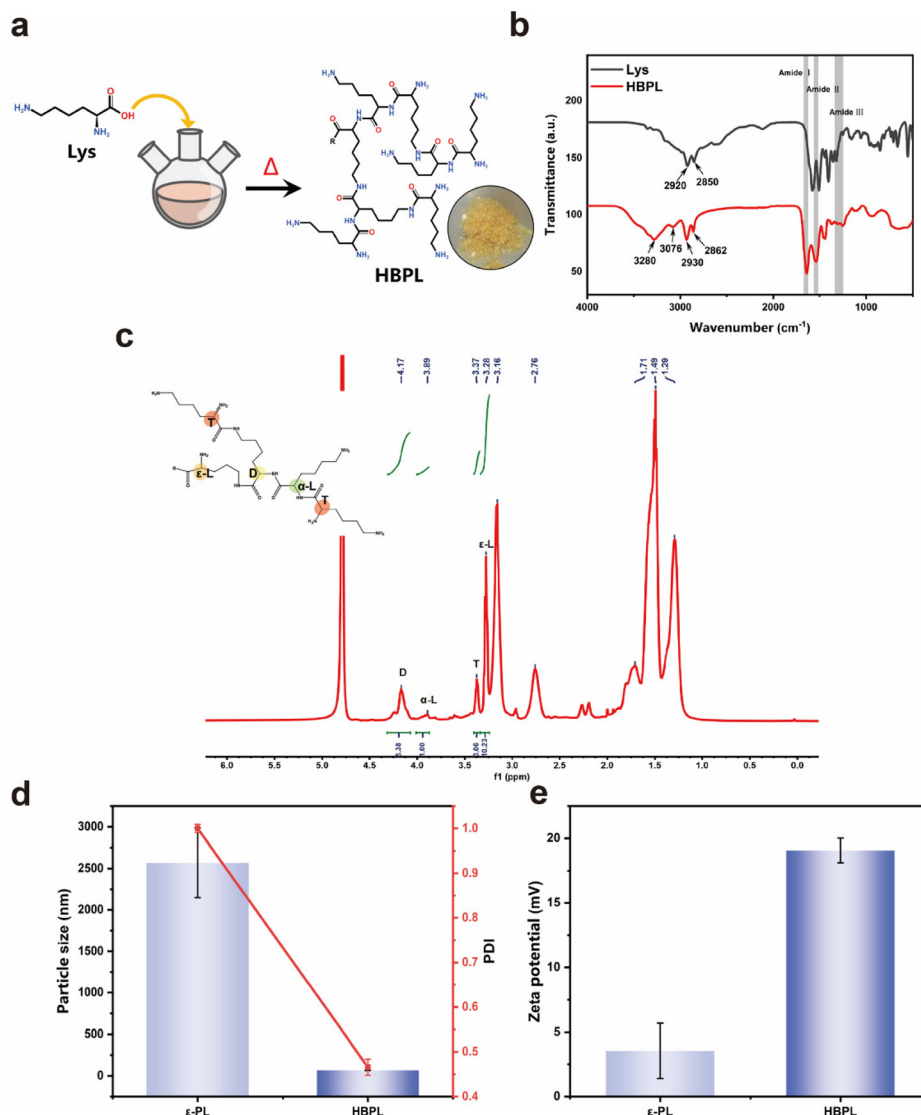


Fig. 4 Preparation and characterization of HBPL. (a) Synthesis process of HBPL. (b) FTIR of Lys and HBPL. (c–e) $^1\text{H-NMR}$, particle size and PDI, and zeta potential of HBPL.

surface through mild chemical treatment, resulting in the fabrication of HBPL-modified sling.

The preparation process of the antibacterial–antiadhesive HBPL-PNE-PP sling is shown in Fig. 5a. Fourier transform infrared spectroscopy (FTIR) confirmed the grafting of PNE and HBPL on the surface of the sling (Fig. 5b). The characteristic peaks of the typical C–C and C–H groups in the saturated carbon chains appeared on the surface of the PP sling. Clearly, PNE-PP exhibited a broad absorption peak in the range of $3700\text{--}3300\text{ cm}^{-1}$, corresponding to the stretching vibrations of N–H and O–H bonds, originating from the phenolic hydroxyl, amino groups, and hydroxyl groups on the hydrocarbon chains of PNE. A new absorption peak appeared at 1646 cm^{-1} , corresponding to the C=C and C–N bonds in PNE, demonstrating the successful polymerization of PNE on the PP surface.⁴⁰ Compared to the infrared spectrum of PNE-PP, after

grafting HBPL, 5HBPL-PNE-PP, 10HBPLL-PNE-PP, 20HBPLL-PNE-PP, and 30HBPLL-PNE-PP showed enhanced characteristic absorption peaks in the range of $3700\text{--}3300\text{ cm}^{-1}$, resulting from the abundant --NH_2 groups in the HBPL molecular structure. The peak intensity increased in the range of $1690\text{--}1640\text{ cm}^{-1}$, corresponding to the --NH_2 and --C=O groups in HBPL, which underwent Schiff base reactions to form --C=N-- double bonds. A new characteristic peak appeared in the amide II region, corresponding to the abundant peptide bonds in the HBPL structure, confirming the successful grafting of HBPL on the PNE-PP surface.

Further analysis of the relative content of chemical elements and chemical states of surface functional groups was carried out using XPS. Fig. 5c shows the XPS spectra of PP, PNE-PP, and 20HBPL-PNE-PP. It can be observed that the N 1s peak appeared in the spectra of PNE-PP and 20HBPL-PNE-PP,

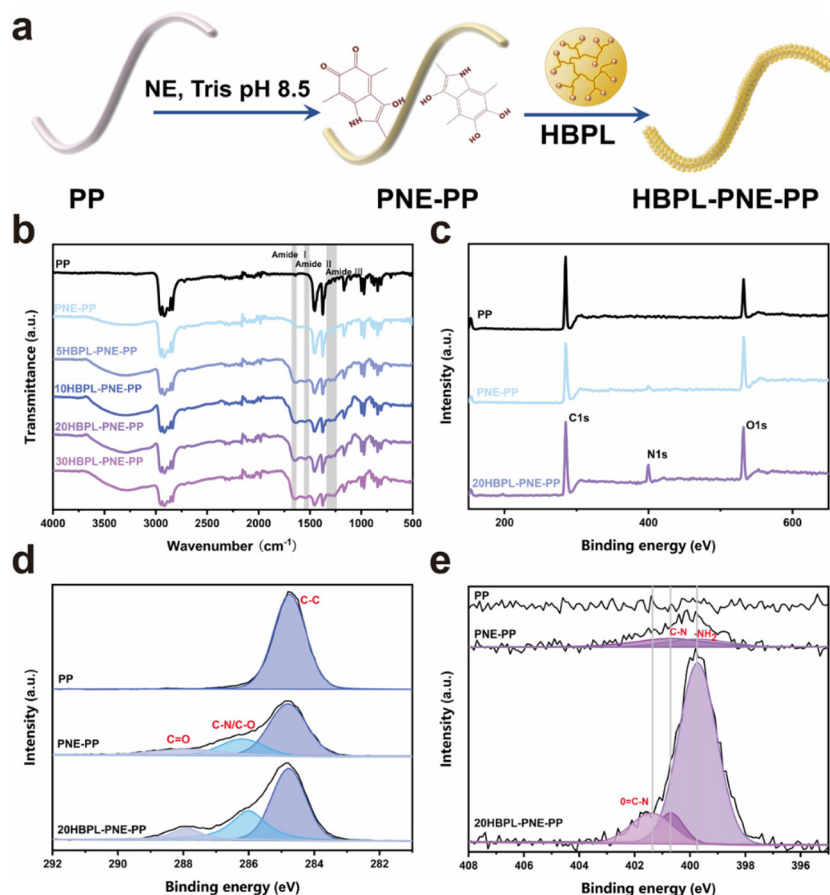


Fig. 5 Construction of coating on sling surface. (a) Preparation process of functionalized sling (b) FTIR. (c–e) XPS survey spectrum, C 1s, and N 1s XPS spectra.

along with a noticeable enhancement of the N 1s and O 1s peaks, confirming the successful grafting of PNE and HBPL on the surface of the PP sling. Combined with Table S1,[†] it can be seen that after grafting HBPL onto PNE-PP, the surface nitrogen content increased from 6.29% to 11.13%, and the C/N ratio decreased from 11.01 to 6.29. This is mainly attributed to the higher nitrogen content in the HBPL molecular structure compared to PNE and PP, further indicating the successful grafting of HBPL with the assistance of PNE.

The C 1s spectrum of 20HBPL-PNE-PP can be fitted into three peak curves at 284.8 eV, 286 eV, and 287.9 eV (Fig. 5d), corresponding to $-C-C$, $-C-N/-C-O$, and $-C=O$ functional groups, respectively. New characteristic peaks of $-C-N/-C-O$ and $-C=O$ appeared in PNE-PP, attributed to the catechol and quinone structures in PNE. Compared to PNE-PP, the spectrum of 20HBPL-PNE-PP exhibited an enhanced peak of $-C=O$, indicating the abundance of amide groups in the HBPL structure. In the N 1s spectrum (Fig. 5e), C–N and NH_2 peaks can be fitted at 400.7 eV and 399.8 eV for PNE-PP, respectively. In 20HBPL-PNE-PP, the NH_2 peak area significantly increased, and a new $O=C-N$ peak appeared at 401.3 eV. This is attributed to the abundant amino groups at the ends of the HBPL hyperbranched three-dimensional structure

and the amide groups in the side chains. It indicates the successful activation and grafting of HBPL particles on the surface of the PP sling through PNE modification.

Fig. 6a shows the macroscopic surface morphology of the original PP sling before and after modification under a biological microscope. After the surface oxidation and self-polymerization of NE to form PNE, the PP monofilament turn into a brown color, which appears uniformly on the front and back side. This color change is attributed to the oxidation of quinones in the aggregated epinephrine particles on the surface. After HBPL grafting, the sling surface remains brown without significant changes.

Fig. 6b presents the microscopic surface coating morphology of the original PP sling, PNE-PP sling, and slings treated with different concentrations of HBPL under SEM. It can be observed that the untreated PP surface is smooth and glossy, while after PNE deposition, a layer of uniformly distributed micro-nano particles attaches to the surface. Under weak alkaline conditions, the phenolic hydroxyl groups of the NE monomer are oxidized and deprotonated to form quinones, which then undergo a reversible Schiff base reaction with the intermediate 3,4-dihydroxybenzaldehyde (DHBA) to produce DHBA-NE through reduction of the imine bond. This sub-

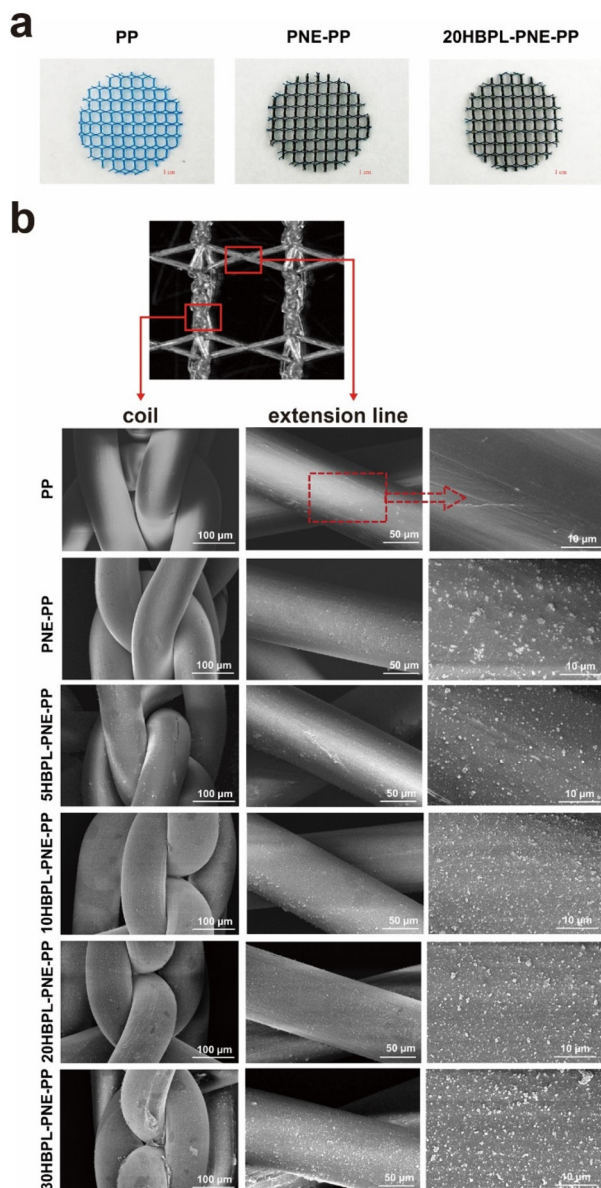


Fig. 6 Characterization of the surface morphology of the samples. (a) Macroscopic morphology of sling after PNE and HBPL modification (b) SEM of slings before and after modification with different HBPL monomer concentrations.

stance slows down the rate of PNE polymerization, allowing the formation of a well-distributed, smooth, and thin PNE coating on the PP surface. The Schiff base reaction between the primary amine groups of HBPL and the quinone groups on the PNE surface introduces antibacterial active molecules of HBPL.^{41,42} When treated with different concentrations of HBPL, the number, and density of particles on the modified PNE-PP surface increase with increasing HBPL concentration. The deposition morphology of the polymer at the coil sleeve and draw line locations vary. At a lower grafting concentration of 5 mg mL⁻¹, HBPL particles grafted at the drawn line are sparsely distributed, and the coating at the coil sleeve is rela-

tively uneven due to the uneven three-dimensional hyper-branched structure of HBPL. With increasing concentrations at 10 mg mL⁻¹ and 20 mg mL⁻¹, both the coil sleeve and draw line locations exhibit densely packed and relatively uniform particles on the monofilament surface. When the grafting concentration reaches 30 mg mL⁻¹, the polymer coating at the coil sleeve becomes rough, gradually accumulating and blocking the mesh pores. Under the deformation of the sling due to stress on the pores, the coating is prone to splitting and detachment.

The HBPL-PNE-PP with the antibacterial and anti-adhesive functionalized coating is mainly achieved through a highly hydrophilic, dense, and uniform surface with cationic bactericidal properties. After HBPL grafting, the polar -NH₂ groups anchored on the PP material surface undergo hydrogen bonding with water in the aqueous environment, gradually altering the surface wettability. Studies have shown that when the end-capped HBPs accumulate on the surface to form a dense structure, the stable interfacial water layer formed by the preferential binding with water molecules acts as a physical barrier against proteins and microorganisms.⁴³ The investigation of surface wettability changes was conducted, and the test results are shown in Fig. 7a. The surface of PP coated with PNE shows an 85.41° decrease in water contact angle (WCA), indicating excellent hydrophilicity of the hydrophobic PP surface, mainly attributed to the presence of amino groups, phenolic hydroxyl groups, and additional hydroxyl groups in PNE. HBPL grafting further affects the surface wettability, with the WCA decreasing to 38.10°, 35.06°, 29.77°, and 27.59° for XHBPL-PNE-PP (X = 5, 10, 20, 30) as the HBPL concentration increases. This decrease is likely attributed to the aggregation of surface particles and an increase in the content of the hydrophilic group -NH₂.

Further quantitative analysis was performed on the surface weight change and grafting amount before and after sling modification, as shown in Fig. 7b. The relative weight increment of the modified sling compared to the original PP material represents the deposition and grafting amount on the surface. It can be observed that the surface grafting amount increases with increasing grafting concentration. Additionally, when the HBPL reaction concentration is 5 mg mL⁻¹ and 10 mg mL⁻¹, the slope of the grafting amount is significantly higher than the two higher concentrations of 20 mg mL⁻¹ and 300 mg mL⁻¹. This suggests that the grafting rate on the surface decreases as the reaction system transitions from low to high concentrations.

The active -NH₂ content on the sling surface not only affects the surface charge, which in turn influences the antibacterial effect but also affects the surface's binding ability with water molecules, thereby influencing bacterial adhesion. Titrations were conducted, and the calculation was based on the difference in NaOH consumption between the experimental samples and the original PP (Fig. 7c) since the PP material surface does not contain active -NH₂ groups. The PNE-PP surface has very few -NH₂ groups and contains a significant amount of quinone and hydroxyl groups, leading to a

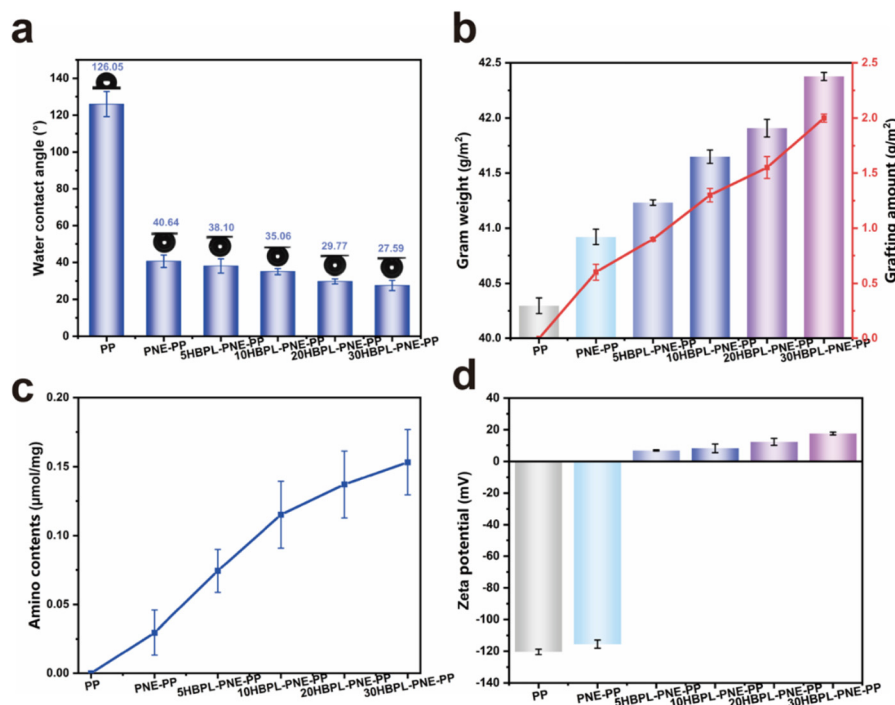


Fig. 7 (a) Water contact angle. (b) Porosity of two types of slings before and after stretching. (c) Amino group content. (d) Zeta potential.

different trend in $-\text{NH}_2$ content compared to the grafting amount test results. Specifically, from PNE-PP to 5HBPL-PNE-PP, the latter has a grafting amount 1.5 times that of the former, while the $-\text{NH}_2$ content is more than 2.5 times higher. Furthermore, at the low grafting concentrations of 5 mg mL^{-1} and 10 mg mL^{-1} , the slope of the $-\text{NH}_2$ content is also higher than the latter two groups, exhibiting a similar trend to the grafting amount results. Overall, as the HBPL concentration increases from 5 mg mL^{-1} to 30 mg mL^{-1} , the $-\text{NH}_2$ content increases from $0.074 \pm 0.016 \mu\text{mol mg}^{-1}$ to $0.150 \pm 0.024 \mu\text{mol mg}^{-1}$, more than five times that of PNE-PP.

Compared to the inert PP material surface, the surface potential of the modified sling is primarily associated with the surface-active functional groups and the physiological pH environment in which it is located. In the human body, the pH of the pelvic compartment is approximately 7.4. When the implanted sling is in the physiological environment, consideration must be given to the site of placement and the implantation pathway. The normal pH of the female vagina ranges from 4.0 to 5.0, while during estrogen fluctuations or bacterial overgrowth, the pH ranges from 5.0 to 6.5. For postmenopausal women, the vaginal pH is above 6.0. Under physiological conditions, the surface zeta potential of the sling before and after modification was tested, as shown in Fig. 7d. The test results indicate that the zeta potential of the original PP sling surface is -120.41 mV , exhibiting a negative charge. After surface modification with PNE, the zeta potential increases to -115.56 mV , attributed to the presence of a small amount of $-\text{NH}_2$ groups on the surface. The abundant $-\text{NH}_2$ groups on the HBPL surface gradually increase the surface zeta potential

of XHBPL-PNE-PP, which are 6.89 mV , 8.15 mV , 12.17 mV , and 17.59 mV , showing a positive charge.

3.3 Antibacterial performance of the sling

Common pathogenic bacteria associated with vaginal mesh infection, such as *E. coli* and *S. aureus*, were selected as representative strains to quantitatively analyze the antibacterial efficacy of the samples. Studies have shown that after the implantation of synthetic materials, the threshold concentration for *S. aureus* infection is reduced to 10^2 – 10^4 CFU mL^{-1} .^{44,45} Merritt *et al.* indicated that *S. aureus* concentrations below 10^6 CFU mL^{-1} can already lead to implant-associated infections.⁴⁶ Xu *et al.* pointed out that the threshold for *E. coli* infection in PP mesh is 10^4 CFU mL^{-1} .⁴⁷ To achieve effective antibacterial coating and prevent bacterial proliferation caused by the mesh, a bacterial suspension concentration higher than the critical threshold of 10^5 CFU mL^{-1} was chosen as the evaluation criterion. The antibacterial effects of the sling before and after modification are shown in Fig. 8a–c. Compared to the original PP, the antibacterial rates of PNE-PP against *E. coli* and *S. aureus* are 26.72% and 65.23%, respectively, indicating that PNE-PP does not possess significant antibacterial effects. The antibacterial rates of 5HBPL-PNE-PP against *E. coli* and *S. aureus* are 67.24% and 78.57%, respectively, demonstrating moderate antibacterial efficacy against *S. aureus* but not against *E. coli*. In contrast, when the grafting concentration increases from 10 mg mL^{-1} to 30 mg mL^{-1} , the antibacterial rates reach 99.99%, showing excellent antibacterial effects and effective inhibition of bacterial growth. This can be attributed to the gradual increase in surface positive

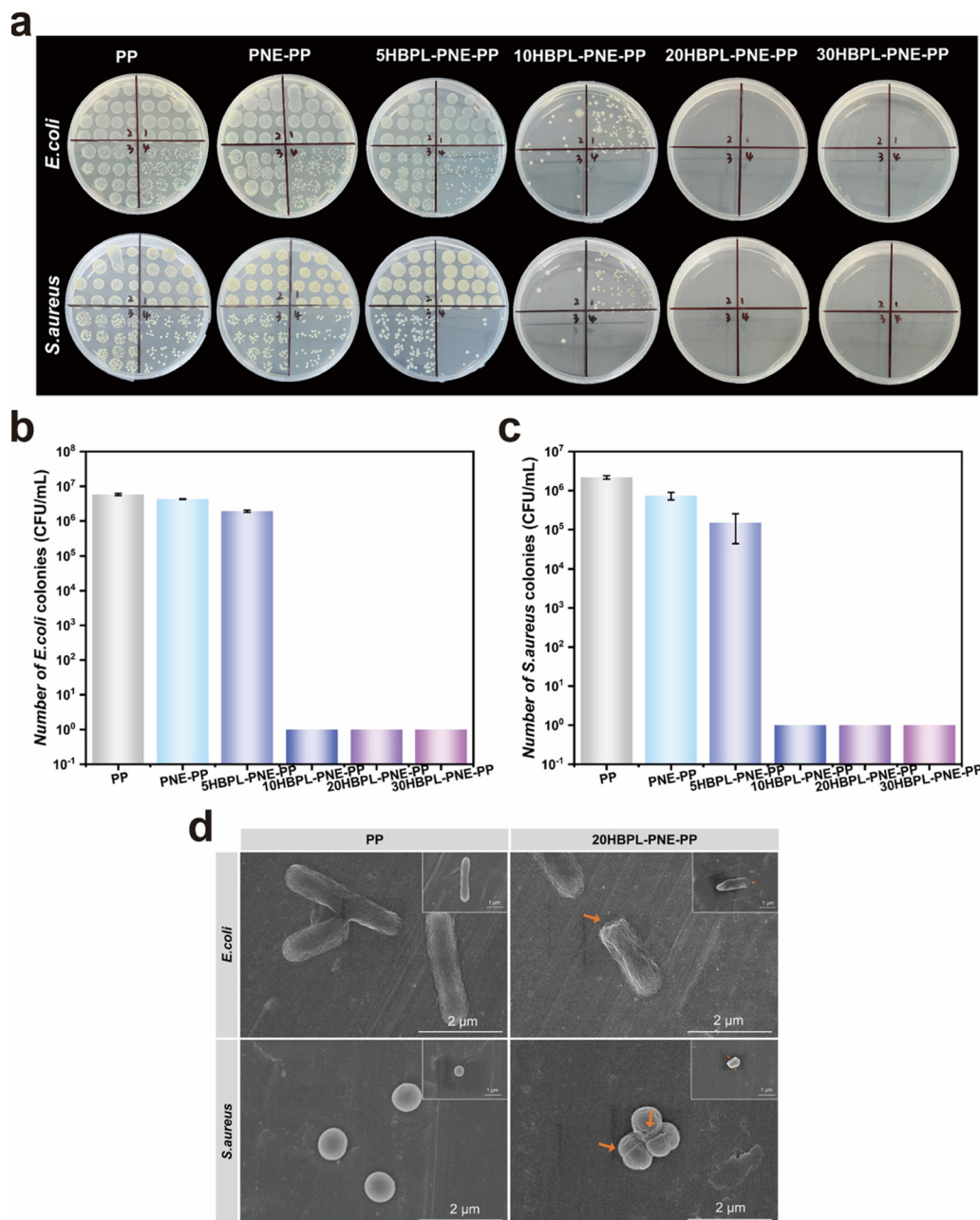


Fig. 8 Antibacterial assessment *in vitro*. (a) *E. coli* and *S. aureus* colonies on different plates. Quantitative numbers of *E. coli* (b) and *S. aureus* colonies (c) on different samples (d) morphology of the adherent *E. coli* and *S. aureus*.

charge. Therefore, 10HBPL-PNE-PP, 20HBPL-PNE-PP, and 30HBPL-PNE-PP, which exhibit excellent antibacterial effects, were further investigated for their surface anti-adhesive properties. It is worth noting that the antibacterial effect of the coating against *S. aureus* is superior to that against *E. coli*, primarily due to differences in bacterial cell membrane composition. Compared to the Gram-negative bacterium *E. coli*, the double-layered membrane structure of the Gram-positive bacterium *S. aureus* has a higher isoelectric point and fewer acidic components.⁴⁸

The morphology and integrity of surface bacteria were observed by SEM. Fig. 8d shows the morphology of surface bacteria before and after sling modification. The results indicate that after co-cultivation with the original PP sling, *E. coli* maintains its intact and elongated rod-like structure, while *S. aureus* exhibits a rounded spherical structure. However, after co-cultivation with the antibacterial surface, the bacteria show wrinkling, deformation, and cell membrane damage. This phenomenon is attributed to the positive surface charge of HBPL, which interacts with the negatively charged bacterial

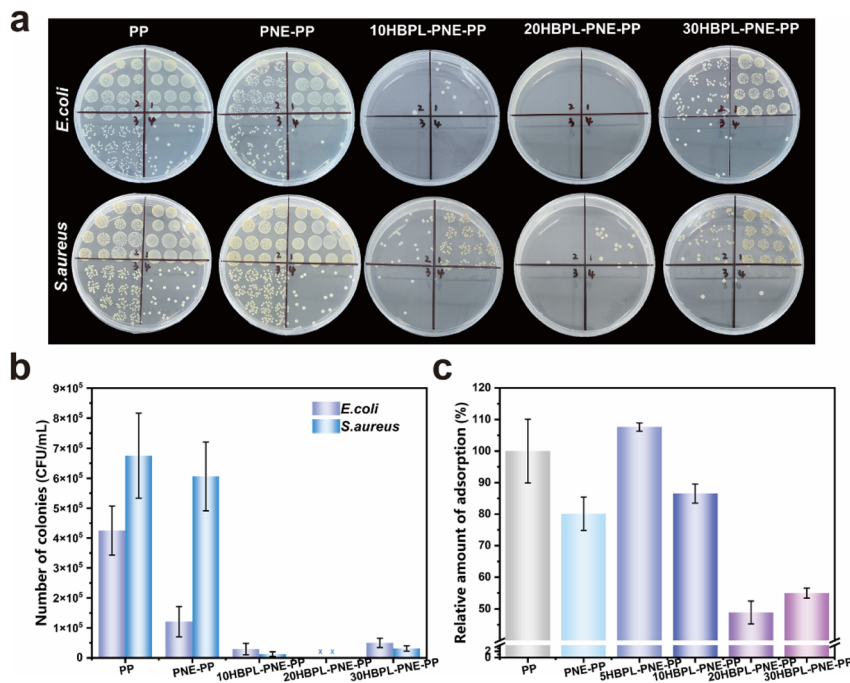


Fig. 9 Anti-bacterial adhesion assessment *in vitro*. (a) *E. coli* and *S. aureus* colonies on different plates. (b) Quantitative numbers of *E. coli* and *S. aureus* colonies on different samples. (c) Anti-protein adsorption amount.

cell membrane through electrostatic interactions at physiological pH. This interference disrupts the permeability of the biofilm, leading to membrane collapse and leakage of cellular contents.⁴⁹

3.4 Anti-adhesive performance of the sling

To compare the anti-adhesive properties of the polymer coatings before and after different grafting concentrations, bovine serum albumin (BSA) was used as a model, and surface protein adsorption was preliminarily evaluated using a BCA protein concentration assay kit. The standard curve for BSA is shown in Fig. S3.† Fig. 9c illustrates the anti-BSA adhesion effect of the sling before and after modification. It can be observed that the protein adsorption on the coating surface is relatively complex. The protein adsorption rate on the PNE-PP surface is 80.12%. This is mainly due to the weak adhesion force and low adhesion energy between BSA and the PNE coating, weakening the intermolecular adhesion.⁴⁹ After treatment with 5 mg mL⁻¹ HBPL, the surface BSA adsorption increases compared to the original PP surface, as the positively charged surface promotes electrostatic protein and bacterial adsorption. As the HBPL concentration increases, the surface BSA adsorption gradually decreases. When the concentration is 10 mg mL⁻¹, the surface protein adsorption decreases to 48.87%. At this stage, the increased number of hydrogen bond acceptor -NH₂ groups on the surface enhances its ability to bind with water molecules. In this case, hydrophilic exclusion from the interface water greatly reduces surface protein adsorption. Long-chain cationic polymer molecules tend to coil, and entanglement between polymer chains reduces the

actual anti-adhesive effect. On the other hand, the three-dimensional hyperbranched molecular structure contains large cavities internally and is less prone to entanglement between molecules. The abundant exposed hydrogen bond acceptors on the surface make the binding with water superior to electrostatic adsorption.⁵⁰ Surprisingly, when the concentration is 30 mg mL⁻¹, the opposite effect occurs, and the protein adsorption rate increases to 54.94%. Studies have shown that under low-concentration conditions, polyelectrolytes deposit on the surface in an extended and stretched manner, resulting in a surface membrane with small roughness and strong hydrophilicity after assembly. In contrast, under high-concentration conditions, polyelectrolytes deposit in an aggregated, increasing the roughness of the surface membrane and affecting its hydrophilicity.⁵¹ Therefore, it is speculated that when the HBPL grafting concentration reaches 30 mg mL⁻¹, cationic polyelectrolytes deposit on the PP surface in an aggregated. Additionally, as shown in Fig. 6b, deposition is better at locations with good flatness, such as the extension lines, while clogging occurs in the loop winding area. Furthermore, the presence of micro-nano protrusions on the material surface can promote the formation of adhesive plaques, and the rough and uneven surface in the loop winding area actually enhances protein adhesion.

To further evaluate the surface anti-bacterial adhesion effect before and after sling modification, the original PP was compared with the three groups exhibiting excellent antibacterial effects. From Fig. 9a and b, it can be seen that compared to PP and PNE-PP, HBPL-PNE-PP shows a similar trend in terms of the anti-bacterial adhesion effect for both *E. coli* and

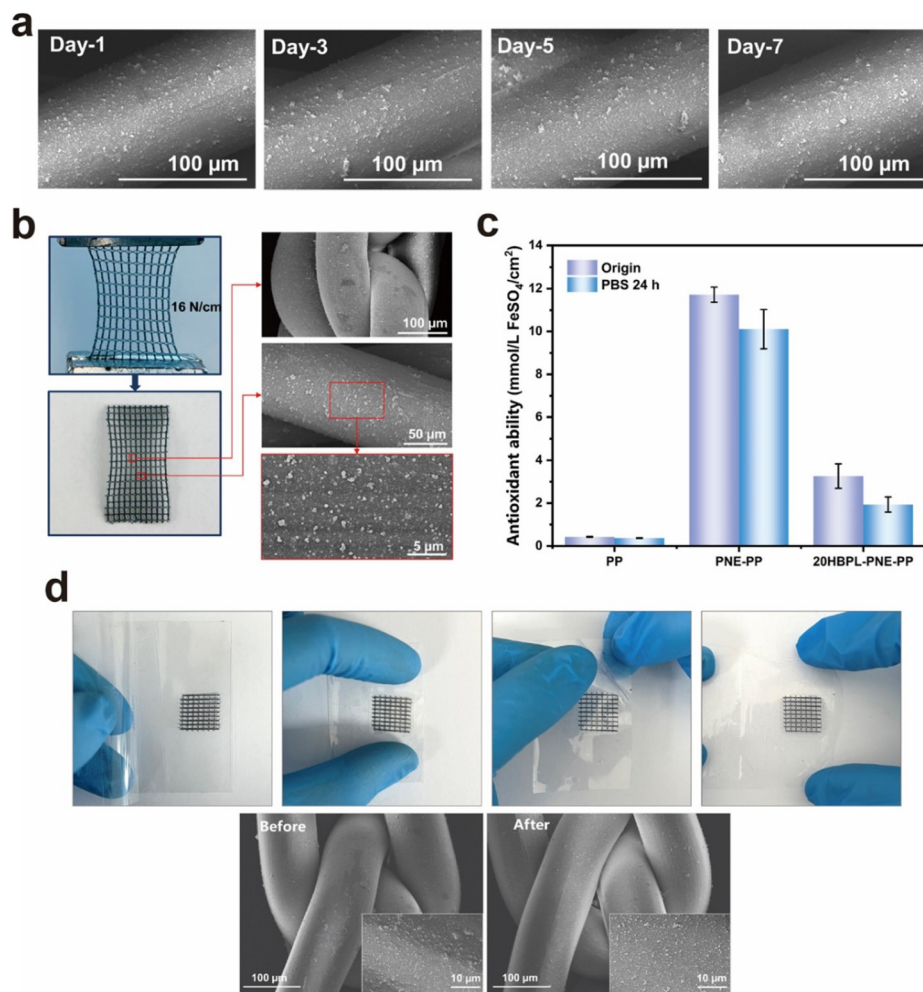


Fig. 10 Coating stability test. (a) *In vitro* degradation test. (b) Tensile stability of the coating. (c) Anti-oxidation. (d) Frictional stability.

S. aureus. Both 10HBPL-PNE-PP and 20HBPL-PNE-PP exhibit surface anti-adhesive efficiency of over 99.9% for the two bacteria. The results show that *S. aureus* adheres to the surface more than *E. coli*, which is attributed to the secretion of more adhesive proteins by *S. aureus*. Taking into account the anti-bacterial effect, 20 mg mL⁻¹ was selected as the optimal HBPL reaction concentration for preparing the antibacterial and anti-adhesive coating on the sling.

3.5 Coating stability

The stability of the coating is crucial for maintaining its composite functionality in the body. A degradation test of the 20HBPL-PNE-PP coating was conducted in PBS (pH 7.4) for 7 days to simulate the effects of body fluids. Fig. 10a shows the SEM images of the modified sling after 1, 3, 5, and 7 days of immersion in PBS. It can be observed that the surface coating of the samples remained intact without any cracking or peeling, demonstrating strong static stability in PBS. Therefore, the coating is minimally affected by the physiological environment, which can be attributed to the stable covalent bonding between HBPL and PNE.

Furthermore, the 20HBPL-PNE-PP sling underwent cyclic tensile testing with a constant load of 16 N cm⁻¹ along the traction direction. Afterward, the surface coating morphology was observed, and the antibacterial test was repeated. The results, as shown in Fig. 10b, indicate that despite slight plastic deformation of the modified sling, the uniformity and density of the polymer nanoparticles on the surface coating at the coil and extension line remained similar to the surface morphology before cyclic stretching, maintaining a uniform and intact coating. Additionally, the antibacterial coating retained excellent antibacterial properties against *E. coli* and *S. aureus*, with antibacterial rates exceeding 99.99% (Fig. S4†).

Considering that the antibacterial and anti-adhesive coating needs to remain stable during the initial stages of wound healing, the oxidative resistance of the coating was investigated. Fig. 10c presents the results of the total antioxidant capacity test before and after sling modification. It can be observed that the PP sling lacks antioxidant capacity, while PNE-PP exhibits antioxidant capacity equivalent to a solution of 11.72 mmol L⁻¹ FeSO₄/cm₂, primarily due to the polyphenolic structure of the PNE surface. After grafting HBPL, the

surface exhibited reduced antioxidant capacity, corresponding to a solution of approximately 3.26 mmol per L FeSO₄ per cm₂. This reduction could be attributed to the oxidation of a substantial portion of the polyphenolic structure, which covalently binds with HBPL.⁴⁰ After immersing the 20HBPL-PNE-PP in PBS for 24 hours to simulate the physiological environment, the antioxidant capacity decreased by 38.83% compared to the initial value. This decrease may be attributed to the oxidation of polyphenolic structures facilitated by oxygen and salt ions in the solution at body temperature. Nonetheless, the coating retained an antioxidant capacity of 2 mmol per L FeSO₄ per cm₂ after 24 h, which is expected to partially mitigate the damage caused by reactive oxygen species (ROS) during the early stages of wound healing when bacterial death occurs.

During surgery, it is inevitable that the sling will undergo bending and folding by the surgeon. As shown in Fig. S5,[†] the polymer coating does not affect the sling's flexibility during arbitrary bending. Some surgical practices involve using a protective sheath to cover the mesh wings of the sling, removing the protective sheath only after securing the pelvic region. This minimizes friction during the surgical procedure. However, the portion near the vaginal mucosa remains exposed and may

experience friction from the surgeon's gloved hand or friction between body tissues during the stress response. By following the steps shown in Fig. 10d, using adhesive tape to adhere to the modified sling, it was observed under SEM that the coating remained intact without detachment, and the surface polymer particles were still densely distributed. This demonstrates the excellent stability of the modified sling's coating under conditions of stronger adhesion than tissue adhesion, indicating that the modified sling's coating stability meets the requirements when in contact with body tissues.

3.6 Cell toxicity

Considering that the sling will be implanted in the pelvic region and come into contact with the human body for a long period, the cell toxicity and proliferation of the multifunctional polymer coating were evaluated using the CCK-8 assay. As shown in Fig. 11a, the absorbance in both the blank wells and test wells increased significantly with the increase in culture days, indicating that cells in the samples before and after sling modification could proliferate normally. The calculation of relative cell viability, as shown in Fig. 11b, revealed that the relative cell viability of all samples exceeded the non-toxic

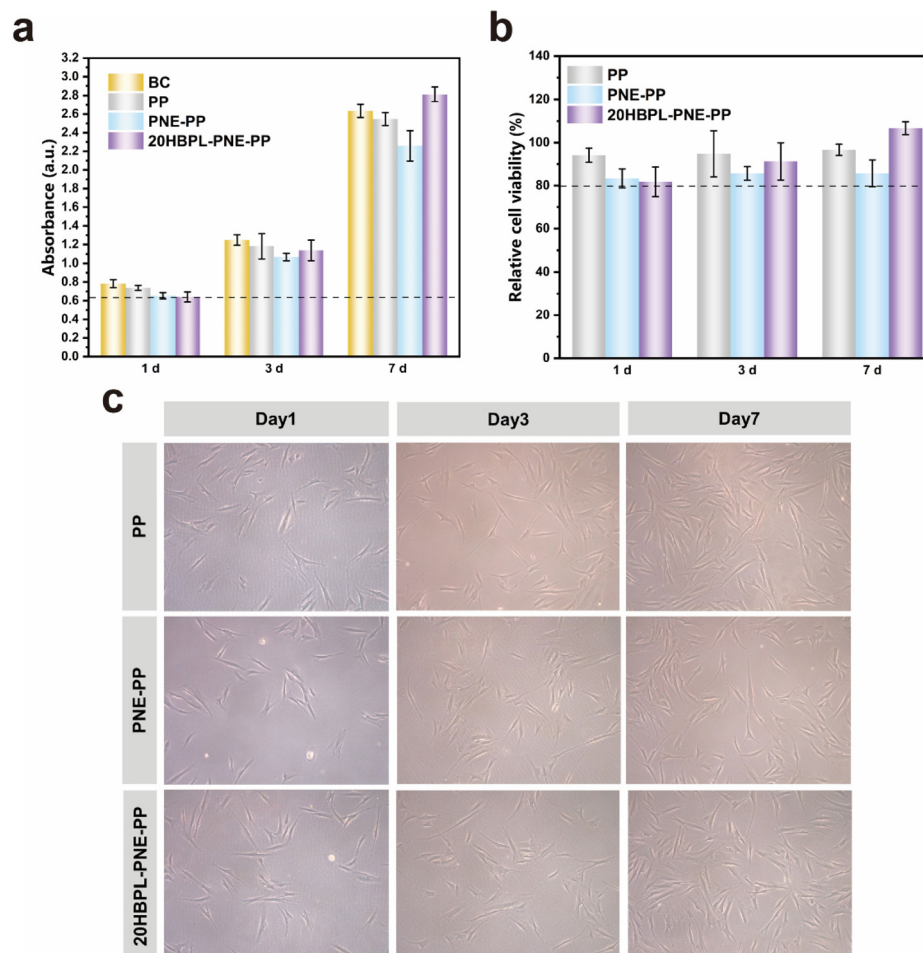


Fig. 11 Cytotoxicity test. (a) UV absorbance of CCK-8 assay. (b) Cell viability. (c) Cell morphology after direct contact.

threshold of 80%, indicating good biocompatibility. The cell viability of the PP sample slightly increased from 94.13% on the first day to 96.65% on the seventh day. The PNE-PP sample exhibited the least increase in cell viability, from 83.37% on the first day to 85.69% on the seventh day. The cell viability of the 20HBPL-PNE-PP sample increased from 81.80% on the first day to 106.73% on the seventh day, surpassing that of PP and PNE-PP. This indicates that the biocompatibility of the sample improved and cell proliferation was promoted after grafting HBPL. Furthermore, microscopic observation revealed that cells in the experimental samples proliferated normally, exhibiting elongated and swirling shapes. No extensive cell vacuolization or clustering of circular dead cells was observed (Fig. 11c).⁵²

4. Conclusions

To address the two main factors influencing postoperative erosion, namely mesh contraction and pore failure, as well as surface bacterial adhesion and colonization, we have developed a lightweight, large-pored, high effective porosity, low contraction rate, and low edge cutting effect sling with antibacterial and anti-adhesive properties. First, from the perspective of textile structure and forming method, we designed a rectangular mesh self-locking edge PP sling and compared it with a commercially available PI 38 sling. Both slings meet the requirements of being lightweight, large-pored, and having a highly effective porosity while ensuring mechanical effectiveness within the body. The PP sling, with its unique structure achieved through the introduction of warp chain organization and weft-inlay yarn, features a rectangular mesh and self-locking edges. This design advantage results in a sling with more stable effective porosity and reduced contraction under TVT and TVT-O procedures, making it potentially achieve a lower erosion rate compared to the commercially available PI 38 sling. Next, based on PP, we performed modification by grafting HBPL onto the inert PP surface using PNE as a mediating layer. By using a grafting concentration of 20 mg mL⁻¹, we successfully prepared a modified PP sling (20HBPL-PNE-PP) with significant antibacterial and anti-adhesive effects. The surface of 20HBPL-PNE-PP is rich in amino groups and positively charged, which exhibits efficient bacterial killing properties. Additionally, the strong hydrophilicity generated by the abundant hydrogen bond acceptors of HBPL creates an interface water-repelling effect, demonstrating excellent resistance to bacterial adhesion *in vitro*. Furthermore, 20HBPL-PNE-PP shows good coating stability, ensuring stable antibacterial and anti-adhesive effects against bacterial growth and adhesion. The coating exhibits excellent biocompatibility and can serve as an effective strategy for constructing antibacterial slings that meet the requirements of vaginal implantation devices, thus potentially contributing to the improvement of postoperative erosion complications. However, in order to further validate the efficacy and safety of our designed sling, future studies using *in vivo* animal models are necessary

to more fully evaluate the effectiveness of the sling for the treatment of stress urinary incontinence in a physiologic setting.

Author contributions

Yan Li: conceptualization, funding acquisition, resources, supervision, writing – review & editing. Shuying Zhao: conceptualization, methodology, validation, formal analysis, investigation, writing – original draft. Meiqi Fang: drawing figures, visualization, investigation. Hao Li: methodology, investigation. Fujun Wang: funding acquisition, resources, supervision. Wang Lu: funding acquisition, resources, supervision.

Conflicts of interest

There are no conflicts to declare.

Acknowledgements

This work was supported by the Fundamental Research Funds for the Central Universities, Grant/Award Numbers: 2232022G-01; Shanghai Science and Technology Development Foundation (21S31900700), Overseas Expertise Introduction Project for Discipline Innovation (111 Project 2.0), Grant No. BP0719035.

References

- 1 Y. Aoki, H. W. Brown and L. Brubaker, Urinary incontinence in women, *Nat. Rev. Dis. Primers*, 2017, 3(1), 17042.
- 2 M. Przydacz, O. E. Y. Adli, W. Mahfouz, O. Loutochin, L. R. Bégin and J. Corcos, Structural differences and architectural features of two different polypropylene slings (TVT-O and I-STOP) have no impact on biocompatibility and tissue reactions, *Cent. Eur. J. Urol.*, 2017, 70(2), 154–162.
- 3 J. M. Wu, A. Kawasaki, A. F. Hundley, A. A. Dieter, E. R. Myers and V. W. Sung, Predicting the number of women who will undergo incontinence and prolapse surgery, 2010 to 2050, *Am. J. Obstet. Gynecol.*, 2011, 205(3), 230.e1–230.e5.
- 4 T. L. Bullock, G. Ghoniem, C. G. Klutke and D. R. Staskin, Advances in female stress urinary incontinence: mid-urethral slings, *BJU Int.*, 2006, 98, 32–40.
- 5 A. A. Berger, J. Tan-Kim and S. A. Menefee, The impact of the 2011 US Food and Drug Administration transvaginal mesh communication on utilization of synthetic midurethral sling procedures, *Int. Urogynecol. J.*, 2021, 32(8), 2227–2231.
- 6 C. M. Gomes, F. L. Carvalho, C. H. S. Bellucci, T. S. Hemerly, F. Baracat, J. D. Bessa, M. Srougi and

- H. Bruschini, Update on complications of synthetic suburethral slings, *Int. Braz. J. Urol.*, 2017, **43**(5), 822–834.
- 7 E. R. Williams and C. G. Klutke, Stress urinary incontinence: the evolution of the sling, *Expert Rev. Med. Devices*, 2008, **5**(4), 507–523.
 - 8 N. Mangir, S. Roman, C. R. Chappl and S. MacNeil, Complications related to use of mesh implants in surgical treatment of stress urinary incontinence and pelvic organ prolapse: infection or inflammation?, *World J. Urol.*, 2020, **38**(1), 73–80.
 - 9 J. G. Blaiva, R. S. Purohit, M. S. Benedon, G. Mekel, M. Stern, M. Billah, K. Olugbade, R. Bendavid and V. Iakovlev, Safety considerations for synthetic sling surgery, *Nat. Rev. Urol.*, 2015, **12**(9), 481–509.
 - 10 C. V. Comiter, Surgery Insight: management of failed sling surgery for female stress urinary incontinence, *Nat. Clin. Pract. Urol.*, 2006, **3**(12), 666–674.
 - 11 C. Eif, B. Jansen, W. Kohnen and K. Becker, Infections associated with medical devices: pathogenesis, management and prophylaxis, *Drugs*, 2005, **65**(2), 179–214.
 - 12 A. Cod, R. Lamberti and S. Martorana, Classification of prosthetics used in hernia repair based on weight and biomaterial, *Hernia*, 2012, **16**(1), 9–20.
 - 13 A. J. Wood, M. J. Cozad, D. A. Grant, A. M. Ostdiek, S. L. Bachman and S. A. Grant, Materials characterization and histological analysis of explanted polypropylene, PTFE, and PET hernia meshes from an individual patient, *J. Mater. Sci. Mater. Med.*, 2013, **24**(4), 1113–1122.
 - 14 S. L. Edwards, J. A. Werkmeister, A. Rosamilia, J. A. M. Ramshaw, J. F. White and C. E. Garget, Characterisation of clinical and newly fabricated meshes for pelvic organ prolapse repair, *J. Mech. Behav. Biomed. Mater.*, 2013, **23**, 53–61.
 - 15 T. Mühl, M. Binnebösel, U. Klinge and T. Goedderz, New objective measurement to characterize the porosity of textile implants, *J. Biomed. Mater. Res., Part B*, 2008, **84B**(1), 176–183.
 - 16 Z. Rusavy, J. Masata, K. Svabik, P. Hubka, K. Zvara and A. Martan, Are the same tapes really the same? Ultrasound study of laser-cut and mechanically cut TVT-O post-operative behavior, *Int. Urogynecol. J.*, 2018, **29**(9), 1335–1340.
 - 17 U. Klinge, B. Klosterhalfen, V. Birkenhauer, K. Junge, J. Conze and V. Schumpelick, Impact of Polymer Pore Size on the Interface Scar Formation in a Rat Model, *J. Surg. Res.*, 2002, **103**(2), 208–214.
 - 18 E. R. Williams and C. G. Klutke, Stress urinary incontinence: the evolution of the sling, *Expert Rev. Med. Devices*, 2008, **5**(4), 507–523.
 - 19 K. M. Knight, G. E. King, S. L. Palcse, A. Suda, R. Liang and P. A. Moalli, Mesh deformation: A mechanism underlying polypropylene prolapse mesh complications in vivo, *Acta Biomater.*, 2022, **148**, 323–335.
 - 20 U. Klinge, B. Klosterhalfen, V. Birkenhauer, K. Junge, J. Conze and V. Schumpelick, Impact of Polymer Pore Size on the Interface Scar Formation in a Rat Model, *J. Surg. Res.*, 2002, **103**(2), 208–214.
 - 21 Z. Rusavy, J. Masata, K. Svabik, P. Hubka, K. Zvara and A. Martan, Are the same tapes really the same? Ultrasound study of laser-cut and mechanically cut TVT-O post-operative behavior, *Int. Urogynecol. J.*, 2018, **29**(9), 1335–1340.
 - 22 O. Guillaume, X. Garric, J. Lavigne, H. V. D. Berghe and J. Coudane, Multilayer, degradable coating as a carrier for the sustained release of antibiotics: Preparation and antimicrobial efficacy in vitro, *J. Controlled Release*, 2012, **162**(3), 492–501.
 - 23 M. Fernández-Gutiérrez, B. Pérez-Khler, S. Benito-Martínez, F. García-Moreno, G. Pascual, L. García-Fernández, M. R. Aguilar, B. Vázquez-Lasa and J. M. Bellón, Development of Biocomposite Polymeric Systems Loaded with Antibacterial Nanoparticles for the Coating of Polypropylene Biomaterials, *Polymers*, 2020, **12**(8), 1829.
 - 24 B. Pérez-Köhler, G. Pascual, S. Benito-Martínez, J. M. Bellón, D. Eglín and O. Guillaume, Thermo-Responsive Antimicrobial Hydrogel for the In situ Coating of Mesh Materials for Hernia Repair, *Polymers*, 2020, **12**(6), 1245.
 - 25 P. Liu, N. Chen, J. Jiang and X. Wen, Preparation and in Vitro Evaluation of New Composite Mesh Functionalized with Cationic Antimicrobial Peptide, *Materials*, 2019, **12**(10), 1676.
 - 26 P. Liu, K. Fu, X. Zeng, N. Chen and X. Wen, Fabrication and Characterization of Composite Meshes Loaded with Antimicrobial Peptides, *ACS Appl. Mater. Interfaces*, 2019, **11**(27), 24609–24617.
 - 27 C. Labay, J. M. Canal, M. Modic, U. Cvelbar, M. Quiles, M. Armengol, M. A. Arbos, F. J. Gil and C. Canal, Antibiotic-loaded polypropylene surgical meshes with suitable biological behaviour by plasma functionalization and polymerization, *Biomaterials*, 2015, **71**, 132–144.
 - 28 K. W. J. Verhorstert, Z. Guler, L. Boer, M. Riool, J. W. R. Roovers and S. A. J. Zaat, In Vitro Bacterial Adhesion and Biofilm Formation on Fully Absorbable Poly-4-hydroxybutyrate and Nonabsorbable Polypropylene Pelvic Floor Implants, *ACS Appl. Mater. Interfaces*, 2020, **12**(48), 53646–53653.
 - 29 H. Patel, D. R. Ostergard and G. Sternschuss, Polypropylene mesh and the host response, *Int. Urogynecol. J.*, 2012, **23**(6), 669–679.
 - 30 A. G. Gristina, Biomaterial-centered infection: microbial adhesion versus tissue integration, *Science*, 1987, **237**(4822), 1588–1595.
 - 31 C. R. Arciola, D. Campoccia and L. Montanaro, Implant infections: adhesion, biofilm formation and immune evasion, *Nat. Rev. Microbiol.*, 2018, **16**(7), 397–409.
 - 32 J. S. Afonso, *Estudo comparativo das propriedades fundamentais das redes de polipropileno usadas no tratamento da incontinência urinária de esforço*, Universidade Federal de São Paulo, 2014.
 - 33 P. Liu, N. Chen, J. Jiang and X. Wen, New surgical meshes with patterned nanofiber mats, *RSC Adv.*, 2019, **9**, 17679–17690.

- 34 C. J. Hawker, R. Lee and J. M. J. Frechet, One-step synthesis of hyperbranched dendritic polyesters, *J. Am. Chem. Soc.*, 1991, **113**(12), 4583–4588.
- 35 D. Höfner, A. Burgath and H. Frey, Degree of branching in hyperbranched polymers, *Acta Polym.*, 1997, **48**(1–2), 30–35.
- 36 U. Klinge, M. Binneboesel, S. Kuschel and B. Schuessler, Demands and properties of alloplastic implants for the treatment of stress urinary incontinence, *Expert Rev. Med. Devices*, 2007, **4**(3), 349–359.
- 37 D. Taylor, The failure of polypropylene surgical mesh in vivo, *J. Mech. Behav. Biomed. Mater.*, 2018, **88**, 370–376.
- 38 Y. Peng, R. Khavari, N. A. Nakib, J. N. Stewart, T. B. Boone and Y. Zhang, The Single-Incision Sling to Treat Female Stress Urinary Incontinence: A Dynamic Computational Study of Outcomes and Risk Factors, *J. Biomech. Eng.*, 2015, **137**(9), 091007.
- 39 S. Brandão, M. Parente, T. H. D. Roza, E. Silva, I. M. Ramos, T. Mascarenhas and R. M. N. Jorge, On the Stiffness of the Mesh and Urethral Mobility: A Finite Element Analysis, *J. Biomech. Eng.*, 2017, **139**(8), 1–9.
- 40 A. Alazzo, T. Lovato, H. Collins, V. Taresco, S. Stolnik, M. Soliman, K. Spriggs and C. Alexander, Structural variations in hyperbranched polymers prepared via thermal polycondensation of lysine and histidine and their effects on DNA delivery, *Int. J. Nanomed.*, 2018, **3**(2), 38–54.
- 41 B. Wang, T. Jin, Q. Xu, H. Liu, Z. Ye and H. Chen, Direct Loading and Tunable Release of Antibiotics from Polyelectrolyte Multilayers To Reduce Bacterial Adhesion and Biofilm Formation, *Bioconjugate Chem.*, 2016, **27**(5), 1305–1313.
- 42 S. Hong, J. Kim, Y. S. Na, J. Park, S. Kim, K. Singha, G.-Il Im, D. Han, W. J. Kim and H. Lee, Poly(norepinephrine): ultrasoft material-independent surface chemistry and nanodepot for nitric oxide, *Angew. Chem., Int. Ed.*, 2013, **52**(35), 9187–9191.
- 43 H. Xu, Y. Cai, X. Chu, H. Chu, J. Li and D. Zhang, A mussel-bioinspired multi-functional hyperbranched polymeric coating with integrated antibacterial and antifouling activities for implant interface modification, *Polym. Chem.*, 2021, **12**(23), 3413–3426.
- 44 H. Cui, W. Wang, L. Shi, W. Song and S. Wang, Superwetable Surface Engineering in Controlling Cell Adhesion for Emerging Bioapplications, *Small Methods*, 2020, **4**(12), 2000573.
- 45 U. Klinge, K. Junge and B. Spellerberg, Do multifilament alloplastic meshes increase the infection rate? Analysis of the polymeric surface, the bacteria adherence, and the in vivo consequences in a rat model, *J. Biomed. Mater. Res.*, 2002, **63**(6), 765–771.
- 46 K. Merritt, V. M. Hitchins and A. R. Neale, Tissue colonization from implantable biomaterials with low numbers of bacteria, *J. Biomed. Mater. Res.*, 1999, **44**(3), 261–265.
- 47 X. Xu, M. Zhan, X. Li, T. Chen and L. Yang, In vivo Analysis of the Resistance of the Meshes to Escherichia coli Infection, *Front. Surg.*, 2021, **8**, 644227.
- 48 G. V. Sherbet and M. S. Lakshmi, Characterisation of Escherichia coli cell surface by isoelectric equilibrium analysis, *Biochim. Biophys. Acta, Biomembr.*, 1973, **298**(1), 50–58.
- 49 Z. Yang, Y. Xi, J. Bai, Z. Jiang, S. Wang, H. Zhang, W. Dai, C. Chen, Z. Gou, G. Yang and C. Gao, Covalent grafting of hyperbranched poly-L-lysine on Ti-based implants achieves dual functions of antibacteria and promoted osteointegration in vivo, *Biomaterials*, 2021, **269**, 120534.
- 50 L. Gao, X. Liu, M. Xu, G. Sun, S. Xu, T. Zou, L. Wang, F. Wang, J. Da, Y. Wang and L. Wang, Biodegradable Anti-Biofilm Fiber-Membrane Ureteral Stent Constructed with a Robust Biomimetic Superhydrophilic Polycationic Hydration Surface Exhibiting Synergetic Antibacterial and Antiprotein Properties, *Small*, 2021, **17**(20), 2006815.
- 51 Y. Ge, P. Li, Y. Guan and C. M. Dong, Hyperbranched polylysine: synthesis, mechanism and preparation for NIR-absorbing gold nanoparticles, *Chin. Chem. Lett.*, 2019, **30**(7), 1428–1431.
- 52 F. D. Lowy, Is Staphylococcus aureus an intracellular pathogen?, *Trends Microbiol.*, 2000, **8**(8), 341–343.